

# A Mechanism for the Response of the Zonally Asymmetric Subtropical Hydrologic Cycle to Global Warming

XAVIER J. LEVINE AND WILLIAM R. BOOS

*Department of Geology and Geophysics, Yale University, New Haven, Connecticut*

(Manuscript received 19 November 2015, in final form 13 July 2016)

## ABSTRACT

Time-mean, zonally asymmetric circulations (hereafter referred to as stationary circulations) maintain intense hydrologic contrasts in Earth's subtropics in the present climate, especially between monsoon regions and deserts during local summer. Such zonal contrasts in hydrology generally increase in comprehensive GCM simulations of a warming climate, yet a full understanding of stationary circulations and their contribution to the hydrologic cycle in present and future climates is lacking. This study uses an idealized moist GCM to investigate the response of subtropical stationary circulations to global warming. Stationary circulations are forced by a prescribed subtropical surface heat source, and atmospheric infrared opacity is varied to produce a wide range of climates with global-mean surface temperatures between 267 and 319 K. The strength of stationary circulations varies nonmonotonically with global mean temperature in these simulations. Zonal asymmetries in precipitation increase with temperature in climates colder than or comparable to that of Earth but remain steady or weaken in warmer climates. A novel mechanism is proposed in which this behavior is caused by the changes in tropopause height and zonal SST gradients expected to occur with global warming. Casting this mechanism in terms of the first-baroclinic mode of the tropical troposphere produces a theory that quantitatively captures the nonmonotonic dependence of stationary circulation strength on global mean temperature. Zonally asymmetric changes in precipitation minus surface evaporation ( $P - E$ ) are predicted by combining this dynamical theory with the tropospheric moisture changes expected if relative humidity remains constant.

## 1. Introduction

Precipitation and surface evaporation exhibit large zonal asymmetries on Earth, with high precipitation rates observed in monsoon regions during local summer but almost no rain seen over continental deserts and oceanic high pressure centers at the same latitude. The largest zonal contrasts in hydrology generally occur in the subtropics and are dynamically set by time-mean zonally asymmetric circulations (hereafter referred to as stationary circulations; e.g., Rodwell and Hoskins 2001; Chou and Neelin 2004; Seager et al. 2010). These stationary circulations are especially prominent in the Northern Hemisphere, where there are large zonal asymmetries in sea surface temperatures (SSTs) and land surface boundary conditions (e.g., Peixoto and Oort 1992). The strength of stationary circulations varies greatly with the seasons, weakening in winter and

strengthening in summer (Shaw and Pauluis 2012; Shaw 2014).

The intimate connection between stationary circulations and zonal asymmetries in hydrology is well established theoretically. For instance, stationary circulations during summer can be accurately simulated when observed precipitation rates are prescribed in dry linear models of the tropical atmosphere (Webster 1972; Hoskins and Karoly 1981; Rodwell and Hoskins 1996). These linear models allow subtropical stationary circulations to be understood as Rossby gyres induced by diabatic heat sources and orography and modified by the zonal-mean basic state in which they occur (Gill 1980; Rodwell and Hoskins 1996). Yet precipitation is strongly influenced by the circulation, so these dry theories cannot be viewed as complete; a full theory would predict winds and precipitation given a distribution of SST or, preferably, distributions of insolation and land-sea boundaries. Nevertheless, it seems clear that the Rossby gyre must be a central element of any successful theory for Earth's subtropical stationary circulations in present, past, or future climates.

---

*Corresponding author address:* Xavier J. Levine, Yale University, 210 Whitney Ave., New Haven, CT 06511.  
E-mail: xavier.levine@yale.edu

Time-mean circulations weaken in comprehensive GCM simulations of future warmer climates (e.g., Tanaka et al. 2004; Vecchi and Soden 2007). For example, simulations of next-century warming predict a weakening of the South Asian monsoon circulation (Douville et al. 2002; Tanaka et al. 2004; Ueda et al. 2006; Cherchi et al. 2011), in qualitative agreement with the weakening of monsoon flows observed in recent decades (Wang and Ding 2006; Zhou et al. 2008). Weakened monsoon circulations are generally accompanied by an increase in monsoon precipitation in simulations of next-century warming, but this precipitation increase occurs at a smaller rate than the increase in atmospheric moisture concentrations (e.g., Ueda et al. 2006; Cherchi et al. 2011).

Aspects of the concomitant weakening of time-mean flow and strengthening of precipitation can be qualitatively understood by considering a radiative–convective equilibrium state subject to globally averaged insolation (e.g., Schneider et al. 2010); an increase in atmospheric longwave opacity in this state would produce a mild increase in tropospheric radiative cooling and latent heat release ( $\sim 2\% \text{ K}^{-1}$ ), but a larger increase in tropospheric static stability and moisture concentration ( $\sim 6\% \text{ K}^{-1}$ ). Global-mean precipitation changes in comprehensive GCM simulations of next-century warming are broadly consistent with this picture, as are global-mean precipitation changes observed in recent decades if one accounts for the radiative effects of clouds and aerosols (Wentz et al. 2007; Zhou et al. 2011; Durack et al. 2012; O’Gorman et al. 2012). A weakening of tropospheric convective mass flux with global warming ( $\sim -4\% \text{ K}^{-1}$ ) follows from these changes in precipitation and moisture or can alternatively be derived from changes in radiative cooling and static stability (Mitchell et al. 1987; Knutson and Manabe 1995; Held and Soden 2006).

Yet how this weakening of the global-mean convective mass flux is partitioned among various components of the circulation is not well understood. For example, tropical stationary circulations weaken more than zonal-mean circulations in simulations of next-century warming (e.g., Joseph et al. 2004; Vecchi and Soden 2007). Global constraints on precipitation and time-mean flow do not constrain regional changes in circulation or precipitation. More generally, local changes in circulation predicted from changes in diabatic heating (e.g., radiative cooling or latent heat release) are of limited use, as local diabatic heating rates are sensitive to local dynamics (e.g., Merlis and Schneider 2011). For this reason, current mechanisms for regional circulation changes that are based on prior knowledge of diabatic heating (e.g., Held and Soden 2006; Ma et al. 2012) can

be useful diagnostics but fall short of being fundamental theories.

Circulation changes are expected to alter regional hydrology as global mean temperature varies, even though a thermodynamic scaling based on the assumption of fixed winds and fixed relative humidity explains important aspects of the changes in the difference between precipitation and surface evaporation ( $P - E$ ) in comprehensive climate simulations of global warming scenarios (e.g., Held and Soden 2006). Regional changes in  $P - E$  are influenced by changes in the strength and horizontal structure of time-mean circulations and transient eddies in simulations of warmer and cooler climate states (Seager et al. 2010; Boos 2012). Dynamical changes are large enough that a purely thermodynamic scaling based on fixed winds can be misleading for some regions experiencing large changes in  $P - E$  (e.g., at the poleward margins of the subtropics; Scheff and Frierson 2012). Understanding regional changes in  $P - E$  thus requires a theory for circulation change, and we posit that understanding the sensitivity of subtropical stationary Rossby gyres to global warming is an important step in building such a comprehensive theory.

Here we propose a novel mechanism relating the strength of subtropical stationary circulations to global mean temperature through two more fundamental quantities: tropical tropopause height and near-surface zonal temperature contrasts. A quantitative theory for the strength of subtropical stationary circulations is obtained by describing this mechanism in terms of a first baroclinic mode of the tropical troposphere. Predictions of the strength of the zonally asymmetric component of  $P - E$  are obtained by combining this theory for stationary circulation with the conventional assumption that lower-tropospheric relative humidity remains unchanged as climate warms. We demonstrate the relevance of these mechanisms to changes in circulation and  $P - E$  using an idealized moist GCM, which is used to simulate climates with a wide range of global-mean surface temperatures.

## 2. Model description

We use an idealized moist GCM that simulates an atmosphere with an interactive hydrologic cycle over an ocean surface having a thermal inertia equivalent to that of 1 m of water (for more details see Frierson et al. 2006; O’Gorman and Schneider 2008). The shortwave albedo of the planet is set to a uniform value, 0.38, which corresponds to Earth’s global-mean Bond albedo. Other constants (rotation rate, gravity, etc.) are kept the same as on Earth. A spectral dynamical core solves for large-scale motions in the atmosphere with a horizontal

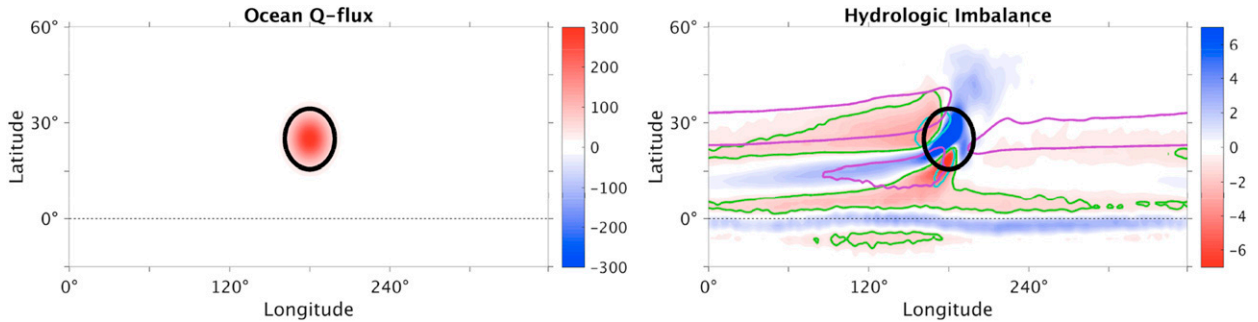


FIG. 1. (left) Spatial distribution of prescribed heat source for all simulations ( $\text{W m}^{-2}$ ). (right) Spatial distribution of the hydrologic imbalance ( $P - E$ ). Color shading shows the reference simulation ( $\text{mm day}^{-1}$ ). Solid contours delimit regions where hydrologic imbalance is drier than  $1.5 \text{ mm day}^{-1}$  for a cold simulation (cyan;  $\langle T_s \rangle = 275 \text{ K}$ ), the reference simulation (green;  $\langle T_s \rangle = 299 \text{ K}$ ), and a warm simulation (magenta;  $\langle T_s \rangle = 315 \text{ K}$ ). Region where the prescribed surface heating exceeds  $50 \text{ W m}^{-2}$  is delimited by the black solid contour. The thin black dashed line indicates the equator.

spectral resolution of T85 and 30 vertical sigma levels ( $\sigma = p/p_s$ , where  $p$  is pressure and  $p_s$  is surface pressure). Water vapor is advected by the flow and condenses when grid-scale saturation occurs. Momentum, moisture, and dry entropy fluxes at the surface are parameterized by bulk aerodynamic formulas; a  $k$ -profile scheme similar to Troen and Mahrt (1986) represents vertical transport by subgrid-scale motions. Moist convection is parameterized by a quasi-equilibrium convection scheme similar to that in Frierson (2007). Radiative heating rates are computed for a gray atmosphere with no clouds, with a constant shortwave optical thickness ( $\tau_{\text{sw}} = 0.22$ ) and a prescribed longwave optical thickness that varies only in height and roughly accounts for longwave absorption by water vapor and well-mixed greenhouse gases:

$$\tau_{\text{lw}} = \tau_e [f_l \sigma + (1 - f_l) \sigma^4], \quad (1)$$

where  $f_l = 0.2$  and  $\tau_e = 7.2$ .

We introduce time-mean zonal asymmetries by prescribing a heat source in the ocean mixed layer of the Northern Hemisphere's subtropics:

$$Q = Q_o \exp \left[ - \left( \frac{\lambda - \lambda_p}{\sigma_{\text{lon}}} \right)^2 - \left( \frac{\phi - \phi_p}{\sigma_{\text{lat}}} \right)^2 \right]. \quad (2)$$

Here,  $\sigma_{\text{lon}}$  and  $\sigma_{\text{lat}}$  define the half-widths in longitude ( $\sigma_{\text{lon}} = 14^\circ$ ) and latitude ( $\sigma_{\text{lat}} = 7^\circ$ ), respectively, for this Gaussian heat source, and  $Q_o$  is its maximum amplitude ( $300 \text{ W m}^{-2}$ ). The heat source is centered at  $\phi_p = 25^\circ \text{N}$  and  $\lambda_p = 180^\circ$  (Fig. 1, left). The heat source alters SST according to the surface energy budget, in combination with all interactive radiative and surface enthalpy fluxes. Introducing a localized surface heating in a moist atmosphere lacking preexisting thermal gradients is analogous to the application of a localized atmospheric heat source in dry simulations of an atmosphere starting

from a state of rest (e.g., Gill 1980; Rodwell and Hoskins 1996). The heat source in our moist GCM is meant to provide an idealization of the summertime land–sea contrast in surface enthalpy fluxes that is caused by the land–sea contrast in surface thermal inertia in Earth's climate; in the real world the ocean is a heat sink during local summer and land is an anomalous source of enthalpy when the zonal mean is removed (e.g., Trenberth and Stepaniak 2004). Alternatively, our ocean heat source could be viewed as a means of supplying the column-integrated energy source that exists over subtropical continents during summer, while avoiding the complexities involved in introducing a land surface into our model.

We alter global mean temperature by rescaling the reference atmospheric longwave optical depth by a spatially uniform factor  $\alpha$ . We use 17 values of  $\alpha$ , from 0.2 to 4, to simulate a wide range of climates for each of two different insolation distributions. Most of this study focuses on simulations with uniform top-of-the-atmosphere (TOA) insolation having a value ( $S_{\text{TOA}} = 340 \text{ W m}^{-2}$ ) nearly equal to that on Earth in the global and annual mean. With this uniform insolation, one simulation is conducted for each value of  $\alpha$  to produce global-mean near-surface temperatures from 267 to 319 K. This range greatly exceeds the approximate 8-K increase in global-mean surface temperature simulated to occur by year 2300 in CMIP5 models under the RCP8.5 emission scenario (Collins et al. 2013). The simulation forced by the reference longwave optical depth ( $\alpha = 1$ ) has a global-mean surface temperature of 299 K, comparable to Earth's tropical SSTs; we refer to this as the reference simulation. We also conduct 17 simulations using the same values for  $\alpha$  but with Earthlike insolation defined by a polynomial approximation of Earth's annual mean insolation  $\{S_{\text{TOA}} = S_o [1 + 0.3(1 - 3 \sin^2 \phi)]\}$ , where  $S_o = 340 \text{ W m}^{-2}$ . Each value of  $\alpha$  is applied in separate integrations that last 2430 and 4860 model days for uniform and Earthlike insolation forcings,

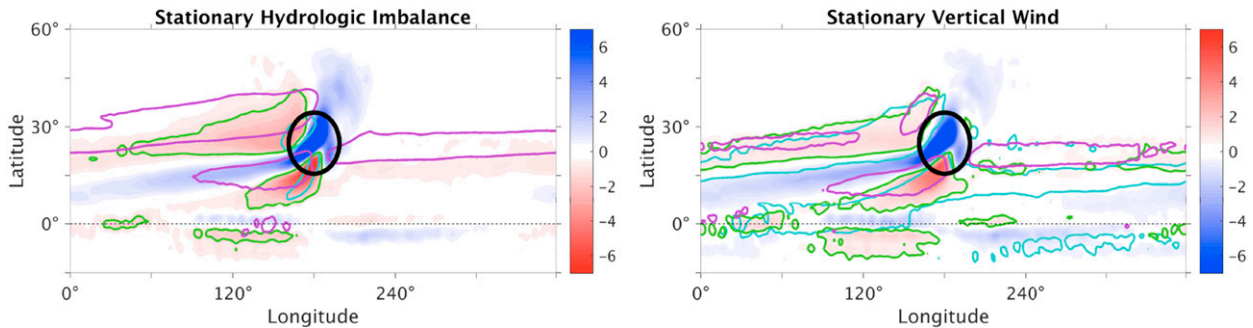


FIG. 2. (left) Stationary hydrologic imbalance (red–blue color shading;  $\text{mm day}^{-1}$ ) in the reference simulation and the  $-1.5 \text{ mm day}^{-1}$  isopleth for the cold, reference, and warm simulations as in the right panel of Fig. 1. (right) Stationary vertical velocity at the 850 hPa level (red–blue color shading;  $10^{-8} \text{ s}^{-1}$ ) in the reference simulation and  $-1.5 \times 10^{-8} \text{ s}^{-1}$  isopleth for the cold, reference, and warm simulations.

respectively. Statistics are accumulated from 4-times-daily samples over the last 1350 and 3780 days in the simulations with uniform and Earthlike insolation, respectively, after a statistical steady state is achieved. A longer averaging time was used for simulations with Earthlike insolation due to larger low-frequency variability in those runs.

### 3. Model results: Uniform insolation

#### a. Reference simulation

To investigate the influence of the subtropical heat source, we examine the time-mean surface hydrologic imbalance (i.e.,  $P - E$ ) and vertical velocity in the reference simulation. Subtropical  $P - E$  has strong zonal asymmetry in the reference simulation (Fig. 1, right), in qualitative agreement with the east–west contrast in Earth’s subtropical Northern Hemisphere during boreal summer and in dry models forced by localized subtropical heating (Rodwell and Hoskins 1996). Wet zones (defined by  $P - E > 0$ ) are most intense over the heat source and extend to the southwest in a comma-shaped region. Dry zones (where  $P - E < 0$ ) extend west and south of the heat source.

There are also weak zonally symmetric bands of positive and negative  $P - E$  just south and north of the equator, respectively. The dry band just north of the equator lies in the subsiding branch of a weak zonal-mean Hadley cell that has its ascent branch over the prescribed heat source. The prescribed heating is not strong enough to induce a cross-equatorial Hadley circulation; instead, a weak quasi-linear Hadley circulation is maintained by the heat source (Plumb and Hou 1992; Zhai and Boos 2015). A second zonal-mean Hadley cell has ascent just south of the equator. This second Hadley cell would exist even in the absence of an imposed subtropical heat source, as convective activity in aquaplanet simulations with uniform SST clusters preferentially along a narrow equatorial band (e.g., Kirtman and

Schneider 2000; Horinouchi 2012). Overall, the zonal-mean circulation is weak and interacts little with the stationary circulation in all climates when there is no meridional insolation gradient.

Figure 2 (left) shows the zonally asymmetric component of the time-mean  $P - E$ , hereafter referred to as the stationary  $P - E$  and denoted  $(P - E)^*$ , where an asterisk represents a time-mean deviation from the time and zonal mean. The spatial distribution of  $(P - E)^*$  strongly resembles that of  $P - E$ , confirming the dominance of zonal asymmetries in the hydrologic cycle. Furthermore, zonal asymmetries in precipitation dominate  $(P - E)^*$ , with evaporation showing less spatial variability (not shown). Regions of positive  $(P - E)^*$  are collocated with regions of stationary ascent, as shown by the distribution of stationary vertical velocity  $\omega^*$  at vertical level  $\sigma = 0.85$  ( $\approx 850 \text{ hPa}$ ; Fig. 2, right).

When defined as regions where either  $(P - E)^*$  or  $P - E$  is smaller than  $-1.5 \text{ mm day}^{-1}$ , dry zones are found to expand poleward and westward as climate warms (Fig. 1, right, and Fig. 2, left). Although choosing the threshold of  $-1.5 \text{ mm day}^{-1}$  is somewhat arbitrary, climate ecosystem classifications are usually based on fixed threshold values for precipitation and evapotranspiration (e.g., Holdridge life zones). Other negative isopleths also show similar westward and poleward expansion with warming, although the  $0 \text{ mm day}^{-1}$  isopleth area does shrink slightly with warming (not shown). A poleward and westward expansion of dry zones is in qualitative agreement with both comprehensive GCM simulations of global warming and observed trends in Earth’s climate over recent decades (e.g., Scheff and Frierson 2012; Li et al. 2012). Using a fixed threshold of  $1.5 \times 10^{-8} \text{ s}^{-1}$  to define regions of strong subsidence (with vertical velocity expressed in the native vertical sigma coordinate), we see that regions of strong subsidence shrink as climate warms, although this trend is not as clear as that of the dry zone expansion due to concomitant changes in the geometry and location

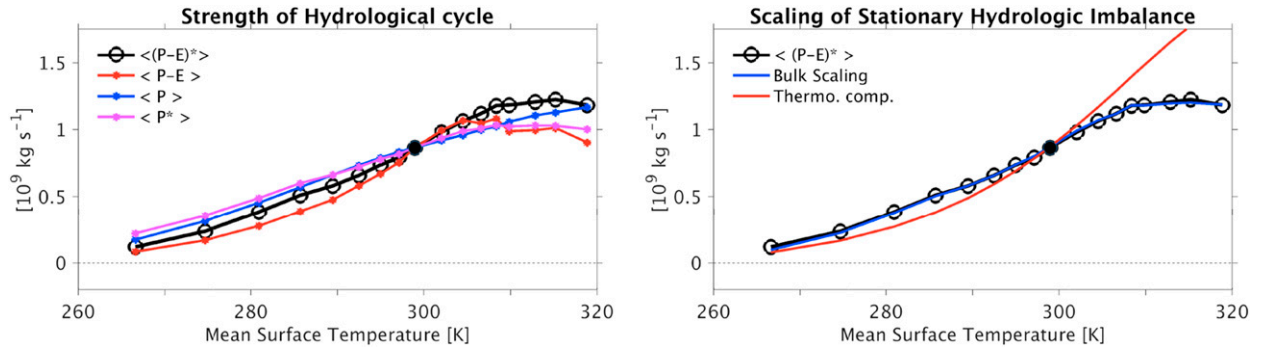


FIG. 3. (left) Bulk stationary hydrologic imbalance  $\langle(P-E)^*\rangle$  (black line), bulk hydrologic imbalance  $\langle P-E \rangle$  (red line), global precipitation  $\langle P \rangle$  (blue line), and bulk stationary precipitation  $\langle P^* \rangle$  (magenta line) vs global-mean surface temperature for each simulation. Global precipitation  $\langle P \rangle$  and bulk hydrologic imbalance  $\langle P-E \rangle$  were rescaled in the reference climate by the bulk stationary hydrologic imbalance  $\langle(P-E)^*\rangle$ . (right) Bulk stationary hydrologic imbalance  $\langle(P-E)^*\rangle$  (black line), its scaling from (6) accounting for both changes in bulk stationary circulation  $\langle\omega^*\rangle$  and averaged saturation specific humidity  $q_r$  (blue line), and that when accounting only for saturation specific humidity changes (red line) vs global-mean surface temperature for each simulation. The filled circles are the reference climate ( $\langle T_s \rangle = 299 \text{ K}$ ).

of subsiding regions. A shrinking of strongly subsiding regions suggests a weakening of the stationary circulation with global warming, consistent with behavior seen in comprehensive GCMs (e.g., Vecchi and Soden 2007).

In summary, we find large zonal asymmetries in the hydrologic cycle in the reference climate, consistent with the stationary circulation induced by the subtropical heat source. The location of subsiding dry zones is qualitatively consistent with that obtained in dry models forced by subtropical tropospheric heat sources (e.g., Rodwell and Hoskins 1996). Dry zones expand with global warming while the stationary circulation weakens. The lack of a strong basic-state Hadley circulation in these simulations precludes a strong influence of zonal mean flow on these changes; these simulations are thus useful for understanding the sensitivity of Earth's subtropical dry zones to global mean temperature because zonal-mean subsidence in the Northern Hemisphere is relatively weak during boreal summer.

### b. Stationary $P-E$ response to global warming

To quantify changes in the strength of zonal asymmetries in the hydrologic cycle, we define a bulk index of asymmetries in  $P-E$  and  $\omega$ . This index is an area integral of positive values:

$$\langle \cdot \rangle = \int_A (\cdot) \mathcal{H}(\cdot) dA. \quad (3)$$

We integrate over all latitudes north of  $1^\circ\text{N}$ ; this large area ensures that (3) captures nearly all of the stationary response to the heat source, which is confined primarily to the subtropical Northern Hemisphere. It excludes a narrow band around the equator for later analytical convenience, as the mechanism proposed in section 4 to explain changes in stationary circulations and  $P-E$

requires nonvanishing values of the Coriolis parameter. The Heaviside function  $\mathcal{H}(\cdot)$  ensures that only positive values are selected, but integrating over only negative values would give identical results when applied to  $\langle(P-E)^*\rangle$  or  $\omega^*$ .

This bulk measure of stationary hydrologic imbalance  $\langle(P-E)^*\rangle$  generally increases with global mean temperature but at very different rates across climates (Fig. 3). From the coldest climate to simulations with global-mean surface temperatures  $T_s$  near 302 K,  $\langle(P-E)^*\rangle$  increases at a relatively fast and steady rate, and then in warmer climates ( $T_s \geq 305 \text{ K}$ ) it becomes nearly invariant with further warming. These changes in  $\langle(P-E)^*\rangle$  are qualitatively similar to those in  $\langle P-E \rangle$ , which includes the zonal-mean component, with both showing a near invariance to changes in global mean temperature in warm climates. Changes in  $\langle P^* \rangle$  also scale similarly, but  $\langle P \rangle$ , which is simply the integrated precipitation, increases in the warmest climates at a much higher rate than  $\langle P^* \rangle$ ,  $\langle(P-E)^*\rangle$ , or  $\langle P-E \rangle$ . This is consistent with global-mean precipitation being constrained by global-mean surface evaporation, which in turn depends on global surface radiative forcings (e.g., O'Gorman et al. 2012); in contrast, we will argue below that dynamical changes influence the strength of zonal asymmetries in the hydrological cycle.

To understand the dynamic and moisture-driven changes in stationary  $P-E$ , we use the steady-state moisture budget to express  $P-E$  in terms of vertical velocity and specific humidity:

$$P-E = \int_{p_s}^0 \nabla \cdot (\mathbf{u}q) \frac{dp}{g} \simeq - \int_{p_s}^0 \omega \partial_p q \frac{dp}{g}. \quad (4)$$

Here,  $q$  is specific humidity,  $\omega$  vertical velocity,  $\mathbf{u}$  is horizontal wind, and  $g = 9.8 \text{ m s}^{-2}$  is the gravitational

acceleration. Equation (4), which shows that moisture flux convergence can be well approximated by vertical moisture advection in column integrals, holds well in the idealized GCM simulations, consistent with horizontal gradients in low-level specific humidity being small in this model. Horizontal humidity gradients are much larger in many places on Earth, but horizontal moisture advection still makes a comparatively small contribution to the dominant spatial patterns of time-mean  $P - E$  in the tropics and subtropics (e.g., Seager et al. 2010, their Fig. 1). From (4), we obtain an expression for stationary  $P - E$ :

$$(P - E)^* \simeq \int_{p_s}^0 \overline{\omega^* \partial_p \bar{q}} \frac{dp}{g}. \quad (5)$$

Here, the overbar defines a zonal mean. Equation (5) assumes that zonal asymmetries in  $P - E$  are set almost entirely by stationary vertical velocities acting on zonal-mean specific humidity. We neglect contributions from transient eddies  $\omega' \partial_p q'$ , zonal-mean flow  $\overline{\omega} \partial_p \bar{q}$ , and stationary eddies in which  $\omega$  and  $q$  covary  $\omega^* \partial_p q^*$ .

Applying the area integration from (3) to (5) provides an expression for the global strength of the stationary  $P - E$  pattern:

$$\langle (P - E)^* \rangle \simeq \text{rh} \int_{p_s}^0 \langle \omega^* \rangle \partial_p \bar{q}_r \frac{dp}{g}. \quad (6)$$

Equation (6) shows that  $\langle (P - E)^* \rangle$  depends on a bulk stationary vertical velocity  $\langle \omega^* \rangle$  and an average saturation specific humidity profile  $\bar{q}_r$ ; rh is an effective relative humidity, which we set to 0.7 to optimize comparison with the diagnosed  $\langle (P - E)^* \rangle$ . Although free-tropospheric relative humidity may vary with climate and its controls remain poorly understood (e.g., Pierrehumbert et al. 2007), comprehensive GCM simulations suggest that its influence on  $\langle (P - E)^* \rangle$  is small compared to that of changes in saturation specific humidity and dynamics (Seager et al. 2010; Boos 2012). The bulk stationary vertical velocity profile is computed by performing the area integration from (3) on  $\omega^*$  at every  $\sigma$  level; its changes are described in section 3c. The average saturation specific humidity profile  $\bar{q}_r$  is computed from an average temperature profile  $T_r$ . We diagnose  $T_r$  in all climates as the averaged temperature profile between 20° and 30°N; this latitude band is chosen to account for the anomalous warming induced by the surface heat source (centered at 25°N). Equation (6) shows that  $\langle (P - E)^* \rangle$  must increase if either the stationary circulation strengthens or tropospheric temperatures increase. The dependence of  $\langle (P - E)^* \rangle$  on global mean temperature is accurately captured by this bulk scaling (Fig. 3, right).

Equation (6) also provides an easy way to quantify dynamic and thermodynamic contributions to changes in stationary  $P - E$ . When  $\langle \omega^* \rangle$  in (6) is fixed at its profile in the reference climate while  $\bar{q}_r$  is allowed to vary, the steady increase in saturation specific humidity with global mean temperature is seen to contribute to the strengthening of stationary  $P - E$  (Fig. 3, right). This thermodynamic scaling provides a decent match to the actual  $\langle (P - E)^* \rangle$  for climates with global-mean surface temperatures less than 302 K but grossly deviates in warmer climates. In the reference climate, for instance, the thermodynamic component increases at a rate of 6.0% K<sup>-1</sup>, compared to only 3.9% K<sup>-1</sup> for  $\langle (P - E)^* \rangle$ . The thermodynamic rate of change is lower than the 7.2% K<sup>-1</sup> increase in column-integrated specific humidity because saturation specific humidity is more sensitive to global warming than the vertical gradient of saturation specific humidity (Betts 1998). This suggests that the near invariance of  $\langle (P - E)^* \rangle$  to temperature in the warmest climates is caused by a weakening of the stationary circulation, which calls for an improved understanding of the controls on stationary circulations.

### c. Stationary circulation response to global warming

To understand the temperature sensitivity of subtropical Rossby gyres induced by off-equatorial heating in a moist atmosphere, we begin by describing the bulk stationary vertical velocity profile  $\langle \omega^* \rangle$ . Stationary vertical velocity peaks in the midtroposphere and decays to zero at the surface and near the tropopause (Fig. 4, left). Its maximum value in the reference climate is 79 Sv (1 Sv  $\equiv 10^6 \text{ m}^3 \text{ s}^{-1}$ ), about half its value in the Northern Hemisphere subtropics during boreal summer on Earth [ $\sim 200$  Sv over the South Asian monsoon region (10°–40°N, 60°–120°E), as obtained from an ensemble of CMIP5 GCM hindcasts averaged over the 1984–2004 period]. As climate warms, the level of maximum  $\langle \omega^* \rangle$  shifts upward, as does the tropopause (Fig. 4, right). Here the tropopause is defined as the level where the tropical-mean lapse rate equals 2 K km<sup>-1</sup>, with this lapse rate diagnosed from the subtropical mean temperature profile  $T_r$  in each climate.

The tropopause shifts from about 500 hPa in the coldest climate to near 10 hPa in the warmest climate. Similarly, the level of maximum  $\langle \omega^* \rangle$  shifts upward from about 800 hPa in the coldest climate to near 400 hPa in the warmest climate (Fig. 4, right). The deepening of the troposphere is associated with an increase of about 50 K in surface temperature, a halving of the tropical lapse rate (from 8 to 4 K km<sup>-1</sup> just above the LCL), and a decrease of 15 K in tropopause temperature (not shown). These changes are consistent with the radiative–convective equilibrium response to increasing longwave opacity and warming SSTs (e.g., Singh and O’Gorman 2012). In addition to undergoing large

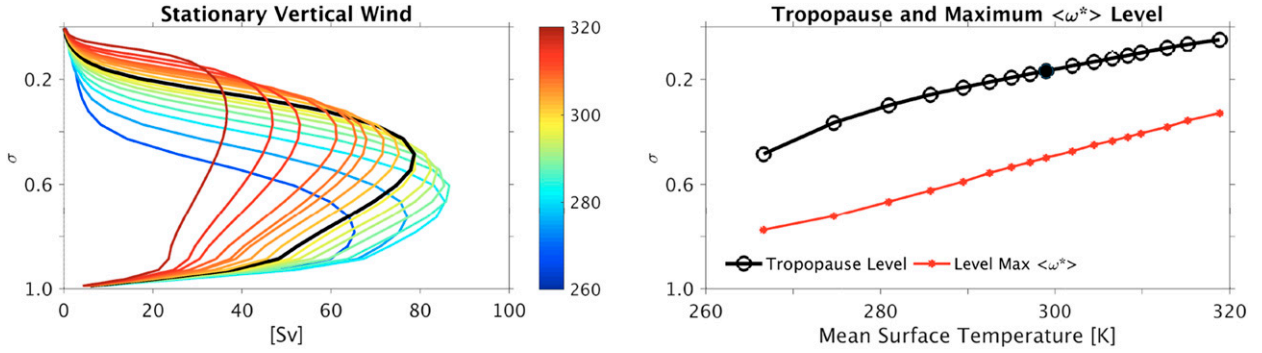


FIG. 4. (left) Bulk stationary vertical velocity profile  $\langle \omega^* \rangle$  for each GCM simulation. Profile colors refer to the global-mean surface temperature of simulations (K), with blue referring to the coldest and red to the warmest climate respectively (reference climate profile is the black line). (right) In sigma levels, the tropopause level (black line) and the level where bulk stationary vertical velocity is maximum (red line) vs global-mean surface temperature. The filled circle is the reference climate.

changes in vertical structure, the strength of  $\langle \omega^* \rangle$  varies nonmonotonically as global mean temperatures increase; it strengthens at most levels in cold climates but then weakens in warm climates. The maximum  $\langle \omega^* \rangle$  is achieved in a relatively cold climate with a global-mean surface temperature near 285 K (Fig. 4, left). The weakening of the stationary vertical mass flux in warm climates offsets the saturation specific humidity increase that occurs as global mean temperature rises, producing the near invariance of stationary  $P - E$  (Fig. 3) for global mean temperatures above 305 K.

Changes in  $\omega^*$  can be constrained using a linear vorticity balance:

$$f \nabla \cdot \mathbf{u}^* = -\beta v^* - g \partial_p (\mathbf{k} \cdot \nabla \times \boldsymbol{\tau}^*), \quad (7)$$

which applies to the subtropical lower troposphere where nonlinearities are generally small (e.g., Wills and Schneider 2015). Here,  $f$  is the Coriolis parameter,  $\beta$  its meridional gradient,  $\mathbf{k}$  the vertical basis vector,  $v$  the meridional wind, and  $\boldsymbol{\tau}$  is the horizontal stress, which is maximum near the surface and decreases rapidly with height. Combining (7) with mass continuity,

$$\partial_p \omega^* = -\nabla \cdot \mathbf{u}^*, \quad (8)$$

provides an expression for stationary vertical velocity:

$$\omega^* = \omega_g^* + \omega_e^*, \quad (9)$$

where

$$\omega_g^* = \frac{\beta}{f} \int_{p_s}^p v^* dp \quad \text{and} \quad (10)$$

$$\omega_e^* \simeq -\frac{g}{f} \mathbf{k} \cdot \nabla \times \boldsymbol{\tau}_s^*, \quad (11)$$

which we refer to as the geostrophic and frictional components of vertical velocity, respectively, and the

subscript  $s$  denotes a property of surface air. Equation (11) holds above the boundary layer, that is, in regions where horizontal stresses are negligible. There, the frictional component of vertical velocity is uniform in height. The geostrophic component in (10), on the other hand, may vary strongly with height through the depth of the troposphere. We approximate  $\omega^*$  by separately integrating its components over areas of stationary ascent:

$$\langle \omega^* \rangle \simeq [\omega_g^*] + [\omega_e^*], \quad (12)$$

where the square brackets denote an integral over regions of stationary ascent, given by

$$[\cdot] = \int_A (\cdot) \mathcal{H}(-\omega^*) dA. \quad (13)$$

Using sums of bulk velocities  $\langle \omega_g^* \rangle$  and  $\langle \omega_e^* \rangle$  would be identical to (12) only if  $\omega_g^*$  and  $\omega_e^*$  each had the same sign as the total stationary vertical velocity. However, the geostrophic and frictional components of ascent sometimes have opposite signs over regions of total stationary ascent in the idealized GCM simulations.

The geostrophic and frictional components obtained from (10) and (11) both contribute significantly to the strength of the stationary circulation in all climates, and both vary nonmonotonically in strength as global mean temperatures increase<sup>1</sup> (Fig. 5, left). The geostrophic component peaks in strength in a climate with global-mean surface temperature of 299 K, while the frictional

<sup>1</sup> To avoid singularities at the equator, we multiply the right-hand side of (13) by  $f$  before horizontally integrating it and then divide the integral by the Coriolis parameter at 25°N. That is, the quantities labeled as  $\langle \omega \rangle$ ,  $[\omega_g^*]$ , and  $[\omega_e^*]$  in Fig. 5 (left) are actually  $\langle f\omega \rangle/f_o$ ,  $[f\omega_g^*]/f_o$ , and  $[f\omega_e^*]/f_o$ . We confirmed that  $\langle f\omega \rangle/f_o$  is nearly identical to  $\langle \omega \rangle$  in all simulations (not shown).

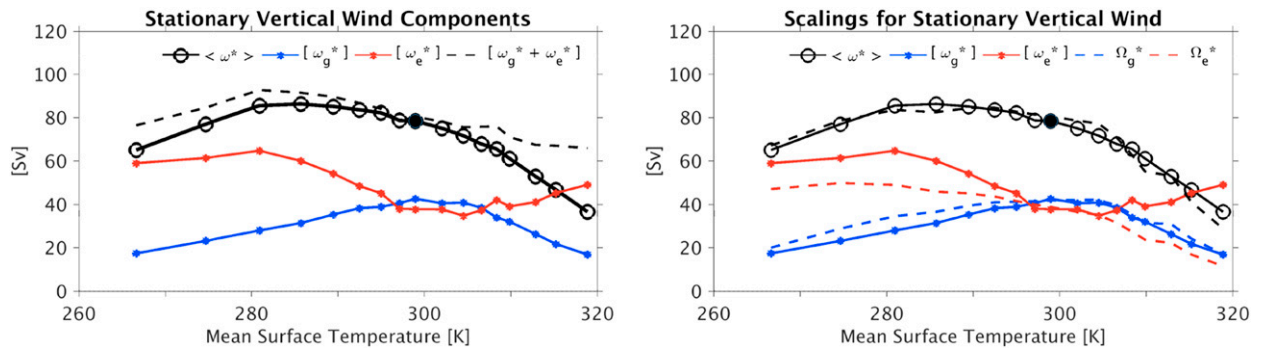


FIG. 5. (left) Bulk stationary vertical velocity  $\langle \omega^* \rangle$  at the level of its maximum (solid black line) and its geostrophic (solid blue line) and frictional component (solid red line) according to the linear vorticity balance (7) vs global-mean surface temperature. Black dashed line is the sum of geostrophic and frictional components. (right) Scalings from (24) for the geostrophic (dashed blue line) and frictional components of bulk stationary vertical velocity (dashed red line) and their combined behavior (dashed black line) vs global-mean surface temperature. Solid lines are as defined in the left panel. The filled circles are the reference climate.

component increases weakly with temperature in the coldest climates then declines as global-mean surface temperature increases from 280 to 310 K and then strengthens again with further warming. The relative contributions of these components to the total mass flux vary greatly with global-mean surface temperature. The nonmonotonic variation in  $\langle \omega^* \rangle$  can thus be associated with the nonmonotonic but quantitatively distinct scalings of geostrophic and frictional stationary circulations, although it is important to note that the decomposition in (9) is diagnostic and does not imply causation. The sum of  $[\omega_g^*]$  and  $[\omega_e^*]$  overestimates  $\langle \omega^* \rangle$  in the warmest climate by almost a factor of 2 (cf. dashed and solid black lines in Fig. 5, left); this discrepancy may be attributed to nonlinearities in the vorticity budget (7).

#### 4. Mechanistic theory

We now propose a mechanism to explain the nonmonotonic dependence of stationary circulation strength on global mean temperature. This, together with the constraint that lower-tropospheric relative humidity does not change, explains the response of  $\langle (P - E)^* \rangle$  to changes in atmospheric longwave opacity. We base our theory on the approximate first-baroclinic vertical structure of tropical and subtropical stationary circulations on Earth (e.g., Trenberth et al. 2000; Chen 2010) and in our idealized GCM (e.g., Fig. 4, left). Although a detailed first-baroclinic-mode framework was derived by Neelin and Zeng (2000, hereafter NZ), we repeat parts of the derivation here because the temperature dependence of the vertical modes, our main focus, was not previously addressed in detail.

As an overview, we will project the stationary vertical velocity onto a first-baroclinic mode and then show that the amplitude of that mode increases as the tropopause lifts in a warming climate. We will also show, using the

linear vorticity balance (7) together with thermal wind balance, that stationary ascent weakens as zonal SST gradients weaken in a warming climate. These two effects—tropopause lifting and the weakening of zonal SST gradients—will be shown to produce the nonmonotonic changes in stationary circulation strength seen in our GCM.

##### a. Projecting ascent on a first-baroclinic mode

As is common in studies of low-latitude dynamics (NZ), we approximate the three-dimensional horizontal wind as the sum of barotropic and baroclinic components; that is,  $\mathbf{u}(\mathbf{x}, p, t) = \mathbf{u}_r(\mathbf{x}, t) + V_1(p)\mathbf{u}_1(\mathbf{x}, t)$ . Here,  $\mathbf{u}_r$  is the horizontal barotropic velocity,  $V_1$  is the vertical structure of the baroclinic mode of the horizontal wind,  $\mathbf{u}_1$  is the local amplitude of the horizontal baroclinic wind, and  $\mathbf{x}$  is the horizontal location. We devise a simple theory for stationary circulations by assuming that horizontal winds are approximately first baroclinic and geostrophic; this assumption holds in our uniform insolation simulations, where the barotropic wind is sufficiently small that the surface value of the stationary meridional wind is nearly equal to the first-baroclinic component of that quantity (not shown). With this assumption, the geostrophic component of vertical velocity (10) becomes

$$\omega_{1g}^* \simeq \frac{p_s}{g} \frac{\beta_o}{f_o} \Omega_1 v_1^*, \quad (14)$$

where  $\Omega_1$  is a vertical structure function defined as

$$\Omega_1 = \frac{1}{p_s} \int_{p_s}^p V_1 dp. \quad (15)$$

Here, the subscript  $o$  on  $\beta$  and  $f$  denotes evaluation at the reference latitude of  $25^\circ\text{N}$ . We refer to  $\Omega_1$  as the vertical wind mode. Similarly, the frictional component of ascent can be constrained by using the bulk

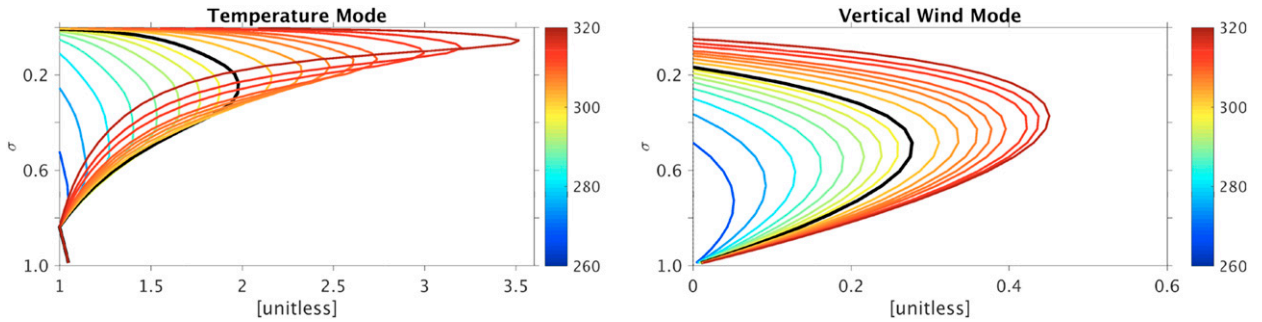


FIG. 6. (left) Temperature mode profile  $A_1$  as defined in (A5) on sigma levels for each GCM simulation. (right) Vertical wind mode profile  $\Omega_1$  as defined by combining (15) and (21) on sigma levels for each GCM simulation. Profile colors are as defined in Fig. 4. Black lines are the reference climate.

aerodynamic formula to approximate the wind stress in (11) in terms of the surface velocity:

$$\tau_s^* = \rho_{rs} \varepsilon \mathbf{u}_s \simeq \frac{p_s}{r_d T_{rs}} \varepsilon \mathbf{u}_1^* V_{1s}. \quad (16)$$

Here  $r_d$  is the specific gas constant of dry air,  $V_{1s}$  is the baroclinic horizontal wind mode evaluated at the surface,  $\varepsilon$  is the drag coefficient, which we assume to be invariant to climate changes, while  $\rho_{rs}$  is surface air density and  $T_{rs}$  is the surface air temperature averaged over the heating region (see averaging convention in the appendix). Assuming that wind stress curl scales linearly with the stationary meridional wind allows the frictional component of the stationary vertical velocity to be approximated as follows:

$$\omega_{1e}^* \simeq \frac{p_s}{r_d T_{rs}} \frac{\varepsilon}{f_o L_p} V_{1s} v_1^*. \quad (17)$$

Here  $L_p$  is the meridional scale of the stationary circulation. The assumed linear scaling between the wind curl and the meridional wind holds for the Rossby gyres simulated in this study, but may not hold when surface meridional winds are weak compared to surface zonal winds. We use the temperature-independent values  $L_p = 600$  km and  $\varepsilon = 0.003$  m s<sup>-1</sup>. Equations (14) and (17) express the dependence of stationary ascent on the stationary meridional wind. Next we will show that the amplitude of the vertical structure of the first-baroclinic mode used in these relations increases as climate warms.

### b. Temperature dependence of the first-baroclinic mode

The existence of the first-baroclinic mode used above is predicated on the moist adiabatic temperature structure of the tropical atmosphere. Large horizontal temperature gradients cannot be maintained in the tropics because of the smallness of the Coriolis parameter there (e.g., Sobel et al. 2001). Temperature can thus be

linearized about a horizontally uniform profile; that is,  $T(\mathbf{x}, p, t) = T_r(p) + \delta T(\mathbf{x}, p, t)$ , where  $T_r$  is the tropical mean temperature profile and  $\delta T$  a local deviation from that profile. An additional constraint is obtained by assuming that deep moist convection acts quickly, relative to the seasonal time scales considered here, to couple local temperature anomalies in the free troposphere to moist static energy anomalies in the subcloud layer (the idea of convective quasi equilibrium; e.g., Neelin 2007). Since the subcloud layer is saturated at its top (the LCL), a free-tropospheric temperature perturbation can then be expressed in terms of perturbations in saturation moist static energy, or temperature, at the LCL:

$$T(\mathbf{x}, p, t) = T_r(p) + A_1(p) T_1(\mathbf{x}, t). \quad (18)$$

Here  $T_1$  is the magnitude of the local temperature anomaly at the LCL and  $A_1$  is the sensitivity of free-tropospheric temperature anomalies to a unit temperature change at the LCL. We refer to  $A_1$  as the temperature mode. Although this modal decomposition of temperature was derived for tropical regions in which the lapse rate is horizontally uniform, it has been used successfully in many studies of subtropical regions (e.g., NZ; Neelin 2007).

An analytical expression for  $A_1$  can be derived (see the appendix), showing that it increases with height to a level just below the tropopause and then decreases toward 0 above this level (Fig. 6, left). Therefore,  $A_1$  is always greater than 1 in the troposphere, and temperature anomalies increase with height in the troposphere above the LCL because of moist convection—a familiar property of the moist adiabat. While our mechanism, which is described below, is highly sensitive to changes in tropopause height, it is influenced little by details of the sensitivity of  $A_1$  to LCL temperature as climate changes.

We now show how  $A_1$  constrains the vertical structure and amplitude of winds. Combining thermal wind balance for meridional winds,

$$f\partial_p v^* = \frac{r_d \partial_x T}{p}, \quad (19)$$

with the modal decomposition for temperature (18), we obtain a solution for the baroclinic wind amplitude, given by

$$fv_1^* = r_d \partial_x T_1, \quad (20)$$

and an expression for the horizontal baroclinic wind mode,<sup>2</sup> given by

$$V_1 = A_1^+ - \frac{1}{p_t - p_s} \int_{p_s}^{p_t} A_1^+ dp. \quad (21)$$

Here,  $p_t$  is tropopause pressure and  $A_1^+$  is defined using the temperature mode:

$$A_1^+ = \int_{p_s}^p \frac{A_1}{p} dp. \quad (22)$$

The wind modes  $V_1$  and  $\Omega_1$  thus depend on only two quantities, the temperature mode  $A_1$  and the tropopause pressure level  $p_t$ , both of which change with tropical mean temperature in ways that can be diagnosed from changes in near-surface temperature and lapse rate. The tropical mean temperature profile, in turn, can be constrained by assumptions about or simulations of the moist convecting state. Figure 6 (right) shows the vertical structure of the vertical wind mode from (15) for each simulation, which we obtained by substituting the temperature mode (Fig. 6, left) and tropopause pressure (Fig. 4, right) into (21) and (22). The vertical wind mode peaks in the midtroposphere and decays to zero at the surface and tropopause, consistent with the horizontal wind mode (21) being of opposite sign in the lower and upper troposphere. Although there are some differences, the vertical structure of  $\Omega_1$  is qualitatively similar to that of  $\langle \omega^* \rangle$  in the GCM simulations, and the large upward shift of the level of maximum  $\langle \omega^* \rangle$  is captured by the temperature dependence of  $\Omega_1$  (cf. Fig. 4, left, and Fig. 6, right).

The vertical wind mode also increases in amplitude with global warming (Fig. 6, right). This has important implications for the sensitivity of the stationary circulation to global mean temperature and is the key result that motivated our detailed discussion of the derivation of  $A_1$  and  $\Omega_1$ . In particular, the amplification of  $\Omega_1$  means that the first-baroclinic-mode dynamics become increasingly sensitive to LCL temperature anomalies as

climate warms. A given horizontal temperature gradient at the LCL will be associated with a stronger baroclinic wind in a warmer climate. Although it will be discussed in greater detail below, we note that the amplitude of  $\langle \omega^* \rangle$  in our GCM simulations increases with global mean temperature only in the coldest climates (Fig. 4, left).

### c. A theory for stationary circulation strength

We can now use this first-baroclinic-mode framework to understand the sensitivity of stationary ascent to a mean warming. We apply the area integral (3) to the geostrophic (14) and frictional (17) components of the stationary vertical velocity and express the meridional wind in terms of the zonal temperature gradient using thermal wind balance (20):

$$\begin{aligned} \langle \omega_{1g}^* \rangle &= r_d \frac{p_s}{g} \frac{\beta_o}{f_o^2} \Omega_1 \langle \partial_x T_1 \rangle \quad \text{and} \\ \langle \omega_{1e}^* \rangle &= \frac{p_s}{T_{rs}} \frac{\varepsilon}{f_o L_p} V_{1s} \langle \partial_x T_1 \rangle. \end{aligned} \quad (23)$$

We introduce the only arbitrary ‘‘tuning’’ parameter in our derivation, a scalar  $\lambda_d$  that expresses the fraction of geostrophic or frictional ascent that contributes to total stationary ascent:

$$\begin{aligned} [\omega_g^*] &\simeq [\omega_{1g}^*] \simeq \lambda_d \langle \omega_{1g}^* \rangle \equiv \Omega_g^* \quad \text{and} \\ [\omega_e^*] &\simeq [\omega_{1e}^*] \simeq \lambda_d \langle \omega_{1e}^* \rangle \equiv \Omega_e^*. \end{aligned} \quad (24)$$

Indeed, geostrophic and frictional ascents are not always collocated, and over many regions they are of opposite sign. We find that  $\lambda_d = 0.6$  provides a good fit in the reference climate, implying that geostrophic ascent is cancelled by frictional descent nearly 40% of the time in our uniform insolation simulations. We assume  $\lambda_d$  to be climate invariant, though there is no obvious reason why this must be true. Although  $\lambda_d$  is a parameter for which we do not have a first-order theory, its climate invariance means that it has no influence on the ability of our scalings to explain relative changes in stationary circulation strength.

The scalings given by (23) and (24) accurately capture the nonmonotonic temperature dependence of the geostrophic component of stationary ascent (Fig. 5, right). They qualitatively capture the weakening of the frictional component with global warming for climates with mean temperature colder than 300 K but fail to capture its strengthening in warmer climates. Further inspection reveals that the poor fit of the scaling for the frictional component arises from changes in the geometry of frictional ascent [i.e., our parameter  $\lambda_d$  in (24); not shown]. Nevertheless, the sum of the geostrophic

<sup>2</sup> A more general derivation of  $V_1$  from the horizontal momentum budget is outlined in NZ.

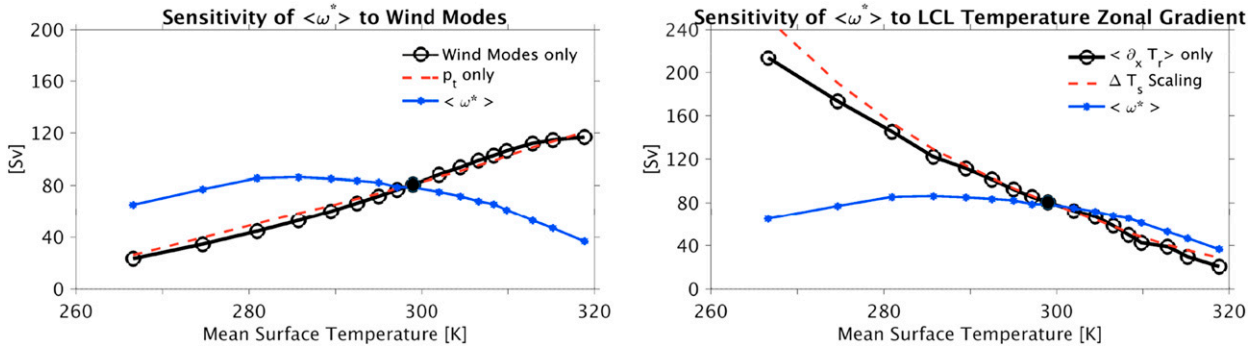


FIG. 7. (left) Contribution of wind modes  $\Omega_1$  and  $V_{1s}$  changes to changes in the bulk stationary vertical velocity  $\langle \omega^* \rangle$  at the level of its maximum value (solid black line) and changes in wind modes  $\Omega_1$  and  $V_{1s}$  resulting from tropopause-level changes only (i.e., temperature mode  $A_1$  is set to its reference climate profile; dashed red line) vs global-mean surface temperature for each simulation. (right) Contribution of bulk LCL temperature zonal gradient  $\langle \partial_x T_r \rangle$  changes to changes in the bulk stationary vertical velocity  $\langle \omega^* \rangle$  at the level of its maximum value (solid black line) and zonal contrast in surface temperature between the heat source and the surrounding ocean (dashed red line) predicted from scaling (25) vs global-mean surface temperature for each climate. Also shown are changes in the bulk stationary vertical velocity  $\langle \omega^* \rangle$  for comparison (solid blue line). The filled circles are the reference climate.

and frictional scalings captures the nonmonotonic changes in stationary circulation strength (cf. solid and dashed black lines in Fig. 5, right). The good fit of the sum of the geostrophic and frictional scalings to the total may be coincidental in the warmest climates or may indicate some error in our diagnosis of the frictional component (recall that the sum of the frictional and geostrophic components provided an overestimate of the total stationary ascent in the warmest climates; see Fig. 5, left).

These scalings help in understanding the cause of the nonmonotonic variations in circulation strength: amplification of the wind modes  $\Omega_1$  and  $V_{1s}$  induces a strengthening of the stationary circulation with global warming (Fig. 7, left), whereas weakening of the LCL zonal temperature gradient  $\langle \partial_x T_r \rangle$  induces a weakening of the stationary circulation (Fig. 7, right). The strengthening of the wind modes is caused almost entirely by the lifting of the tropopause. Indeed, the change in the wind modes is nearly identical to that obtained when prescribing the temperature mode to its reference simulation profile in (21) and (15), as shown in Fig. 7 (left; cf. dashed red and solid black lines). Thus, the sensitivity of  $A_1$  to tropical mean temperature produces negligible change in the stationary circulation. The lifting of the tropopause amplifies ascent in two ways: 1) it provides a deeper layer over which a given amount of horizontal convergence is integrated vertically to produce, via mass continuity, larger mid-tropospheric vertical velocities, and 2) it increases the amplitude of horizontal convergence in the upper and lower troposphere by amplifying horizontal geopotential height gradients there. The second effect occurs because a given horizontal temperature gradient is associated with a

larger thickness gradient in a layer containing more mass (e.g., the hypsometric equation).

The weakening of the LCL temperature gradient  $\langle \partial_x T_r \rangle$  with global warming is associated with a weakening of the SST gradient. Boundary layer mixing efficiently communicates SST anomalies to the LCL. When the lapse rate of the subcloud layer and LCL height are nearly invariant to climate change, as they are in our simulations, LCL temperature anomalies scale linearly with SST anomalies. Merlis and Schneider (2011) devised a simple scaling for the strength of a tropical SST gradient [see also Knutson and Manabe (1995), who found evaporative cooling to control zonal SST contrast in the equatorial Pacific in a model with a dynamical ocean]:

$$\Delta T_s \sim \frac{\Delta Q}{\partial_T q_{rs}}. \quad (25)$$

Here,  $\Delta T_s$  is the SST difference between two horizontal locations and  $\Delta Q$  is the difference in surface latent heat flux. The saturation specific humidity at the surface  $q_{rs}$  is computed from near-surface air temperature around our heat source (i.e., averaged between 23°–27°N and 175°–185°E). Merlis and Schneider (2011) obtained (25) by expressing  $\Delta Q$  in terms of zonal anomalies in  $q_{rs}$  using the bulk aerodynamic formula; an SST anomaly  $\Delta T_s$  was then obtained by linearizing the near-surface specific humidity anomaly in temperature. The scaling from (25) applies to a regime in which SST responds directly to the prescribed heating, without influencing changes in surface wind speed or relative humidity. To apply this to our simulations, we assume that  $\Delta Q$  is given by our imposed subtropical heat source (2); since  $\Delta Q$  is invariant to climate change in our simulations, (25)

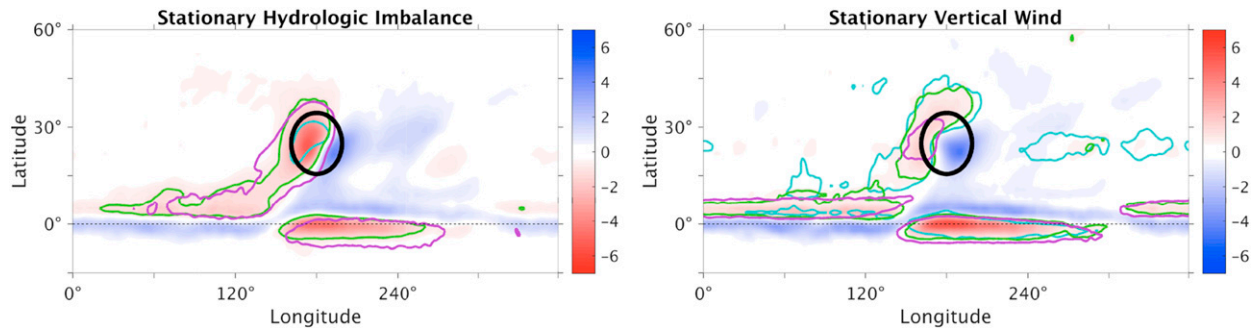


FIG. 8. As in Fig. 2, but for Earthlike insolation simulations.

predicts a decrease in the magnitude of the SST anomaly with global warming following the fast increase of near-surface specific humidity and its horizontal gradients. We find that SST changes predicted from (25) accurately capture the rapid decrease in LCL zonal temperature gradient with global warming (cf. dashed red and solid black lines in Fig. 7, right). We rescaled  $\Delta T_s$  to equal  $\langle \partial_x T \rangle$  in the reference simulation, so this agreement indicates that the scaling successfully predicts the relative changes, but not necessarily the mean magnitude.

In summary, the scalings from (23) and (24) explain the nonmonotonic changes in the strength of the stationary circulation. These changes result from a competition between the deepening of the troposphere, which strengthens the stationary circulation, and the weakening of zonal temperature gradients in the lower troposphere, which weakens the stationary circulation. Changes in the wind modes  $\Omega_1$  and  $V_{1s}$  are produced almost entirely by changes in tropopause level, while changes in LCL zonal temperature gradients are controlled by SST changes.

### 5. Model results: Earthlike insolation

We now investigate the relevance of our findings to simulations forced by an insolation profile resembling Earth's in the annual mean, with the same subtropical heat source as before. These simulations bear much greater resemblance to Earth's annual-mean climate, with strong zonal-mean circulations in the tropics and extratropics (O'Gorman and Schneider 2008; Levine and Schneider 2011). The heat source is centered in the subtropical dry zones, where zonal-mean  $P - E$  is negative and zonal-mean subsidence occurs. Despite the presence of strong Hadley cells in the tropics and storm tracks in the extratropics, the stationary vertical velocity and  $P - E$  have distributions similar to those found in the uniform insolation scenario, with wet stationary ascent east of the heat source and dry subsidence to the west (Fig. 8, cf. Fig. 2; storm tracks are not visible because they project strongly on the zonal mean, which has

been removed in these figures). When using the same  $-1.5 \text{ mm day}^{-1}$  threshold for  $(P - E)^*$  as for the uniform insolation simulations, dry zones are found to expand poleward and westward as climate warms in climates colder than the reference simulations but barely vary or even shrink in warmer climates<sup>3</sup> (Fig. 8, left). This behavior is associated with a shrinking of regions of strong subsidence with global warming in simulations warmer than the reference climate (Fig. 8, right). These similarities between the Earthlike and uniform insolation simulations are consistent with dry studies, which found the stationary Rossby wave response to a subtropical heat source to be qualitatively preserved in basic states with a range of zonal-mean flows (e.g., Rodwell and Hoskins 1996).

To see whether differences in the basic state affect the temperature sensitivity of stationary  $P - E$  and vertical velocity, we examine the same set of metrics used for the uniform insolation simulations. With Earthlike insolation,  $\langle (P - E)^* \rangle$  shows a rapid increase with global warming for global-mean surface temperatures less than 305 K but then declines with further warming (Fig. 9). This is qualitatively similar to the sensitivity with uniform insolation but with a stronger weakening in the warmest climates. The term  $\langle (P - E)^* \rangle$  in the Earthlike simulations is also weaker than in the uniform insolation simulations; this difference is attributable to subtropical zonal temperature gradients at the LCL being weaker in the Earthlike insolation simulations, despite zonal contrasts in SST being comparable to those in the uniform insolation simulations. Presumably, temperature is homogenized by the much stronger zonal-mean zonal wind in the integrations with Earthlike insolation. As with

<sup>3</sup> Nevertheless, dry zones as defined from total  $P - E$  expand with global warming, consistent with changes in hydrology and circulations becoming more zonally symmetric. This zonalization with global warming is apparent in comprehensive GCM simulations as well (e.g., Joseph et al. 2004).

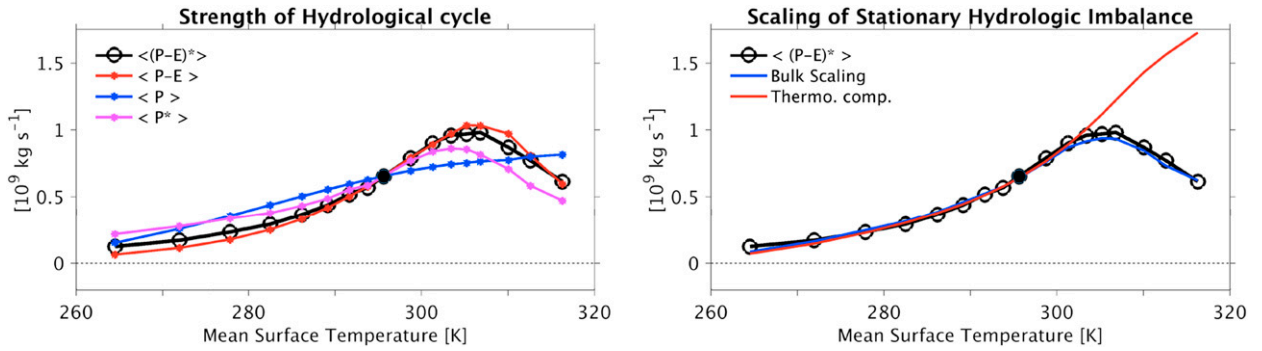


FIG. 9. As in Fig. 3, but for Earthlike insolation simulations.

uniform insolation, spatially integrated total precipitation  $\langle P \rangle$  scales almost linearly (Fig. 9, left) and saturated specific humidity near exponentially with temperature (Fig. 9, right) over the entire range of climates.

The bulk stationary vertical velocity has nearly a first-baroclinic structure in the basic state with Earthlike insolation and also exhibits a nonmonotonic dependence on global mean temperature (Fig. 10, left). This nonmonotonic behavior is approximated by our scalings (23) and (24) for the geostrophic and frictional components of ascent (Fig. 10, right). Following the scaling from (25), zonal SST contrast decreases as climate warms, and the LCL zonal temperature gradient scales linearly with the zonal SST gradient. In applying these scalings, we used the slightly smaller values of  $\lambda_d = 0.5$  and  $\varepsilon = 0.0020 \text{ ms}^{-1}$ , with the lower drag coefficient justified by the fact that surface winds are weaker in the simulations with Earthlike insolation. The stationary flow in these simulations also has a large barotropic component that seems to arise from a zonal tilt in the stationary response to the subtropical heat source: the upper-level anticyclone is shifted east of the lower-level cyclone (not shown), presumably as a result of the strong eastward vertical wind shear in the extratropics of the basic state. Although the effect of this basic state flow on the temperature sensitivity of the response certainly merits further examination, the fact that the same core structure of a baroclinic Rossby wave still exists may

explain why the qualitatively similar response of the stationary circulation is seen in the two different basic states and why it can be at least roughly approximated by theoretical scalings for a first-baroclinic Rossby wave.

6. Conclusions

Much previous work has examined the global- and zonal-mean response of precipitation and circulation to changes in global mean temperature (e.g., Held and Soden 2006), but the response of the zonally asymmetric part of the flow has been studied relatively little. Zonally asymmetric circulations are particularly relevant in the subtropics during local summer, where they set the strong hydrological contrast between monsoon regions and either continental deserts or oceanic highs at the same latitude. Although the dry, linear response to an imposed, zonally confined heat source has for decades served as a cornerstone of our understanding of the most prominent zonal asymmetries in Earth’s climate (e.g., Gill 1980; Rodwell and Hoskins 1996), the generalization of that idealized response to a moist framework and its sensitivity to global mean temperature have remained open issues.

Here we used a moist idealized GCM to simulate the response to a prescribed subtropical surface heat source under a wide range of atmospheric infrared opacities. This heat source induces a baroclinic stationary circulation qualitatively similar to that obtained in dry

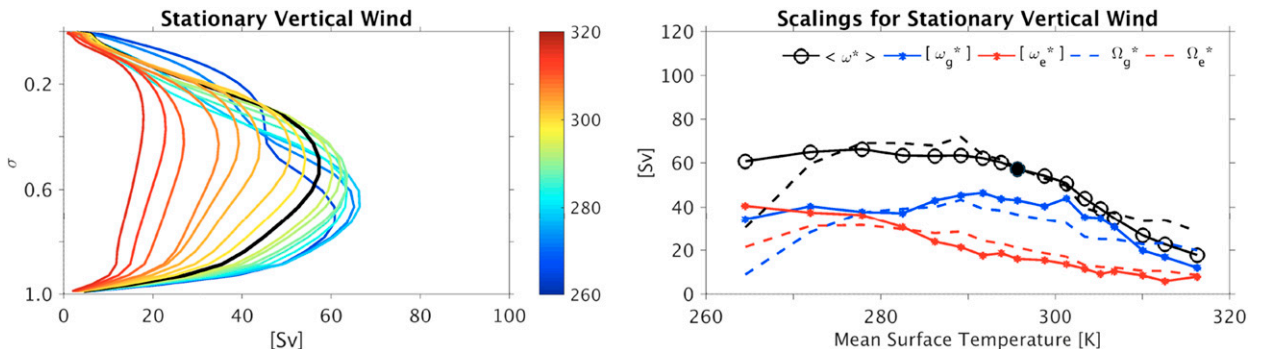


FIG. 10. (left) As in Fig. 4 and (right) as in Fig. 5, but for Earthlike insolation simulations.

models: there are cyclonic motions in the lower troposphere and anticyclonic motions in the upper troposphere, zonally confined precipitating ascent east of the heat source, and zonally elongated subsidence to the west. Bulk metrics show that the zonally asymmetric component of the circulation varies nonmonotonically as climate warms, reaching its maximum value in a relatively cold climate. For climates with global mean temperatures near that of present-day Earth, the stationary circulation steadily weakens with global warming, in qualitative agreement with the weakening of stationary circulations found in comprehensive GCM simulations of the next century (e.g., Vecchi and Soden 2007).

Our central result is a new quantitative theory, phrased in terms of the first-baroclinic mode of the tropical troposphere, for the sensitivity of the stationary circulation to global mean temperature. This theory attributes the nonmonotonic circulation changes to a competition between a weakening of the zonal SST gradient, which dominates to weaken the circulation in very warm climates, and a deepening of the tropical troposphere, which dominates to strengthen the circulation in cold climates. This theory is based on standard assumptions for the surface energy budget and thermal stratification of the tropical and subtropical troposphere, together with a commonly used treatment of tropical first-baroclinic mode dynamics (e.g., NZ). It is novel not only in its application to the stationary circulation but also in its dynamical treatment of the changes that happen in a warming tropical or subtropical troposphere. That is, most theories for tropical circulation changes rely on the energy budget or the thermodynamic equation, in which diabatic or moisture sources are prescribed, to explain how the temperature dependence of moist adiabatic lapse rates or tropopause height influence time-mean tropical circulations (e.g., Held and Soden 2006; Ma et al. 2012). Chou and Chen (2010) argued that tropopause lifting may influence circulations but invoked the effect of this lifting on the gross moist stability as the central mechanism. Our theory is instead based on the horizontal momentum equation and shows how tropopause lifting produces an increase in lower-tropospheric horizontal convergence and midtropospheric ascent, given a fixed near-surface horizontal temperature gradient.

In our simulations, the temperature dependence of zonal asymmetries in  $P - E$  was accurately described by combining the nonmonotonic changes in the strength of the stationary circulation with a Clausius–Clapeyron scaling for specific humidity. Specifically, the zonally asymmetric component of time-mean  $P - E$  increases rapidly with warming in cold climates, where the increase in the vertical gradient of saturation specific humidity dominates, and then becomes nearly invariant

(or even decreases) with further warming in warm climates as the weakening circulation compensates for the continued increase in saturation specific humidity.

This mechanism for changes in subtropical stationary circulation and  $P - E$  was found to operate even in simulations forced by Earth's annual-mean insolation profile, even though the zonal-mean flow introduced some alterations to the basic response to the subtropical heat source. Since Earth's monsoon circulations usually occur in relatively weak summer zonal-mean flows, it is possible that the simulations with uniform insolation are more relevant to observed subtropical zonal asymmetries than the simulations with Earthlike insolation. Regardless, our theoretical scalings rely on general assumptions for the tropical and subtropical atmosphere, and it may be possible to adapt these to contexts beyond that of the subtropics; for example, one could use a dissipative momentum balance in the deep tropics or introduce a term into the momentum balance to represent interaction with a zonal-mean basic state. Complications arising from interactions with land surface boundary conditions and topography may be even more important, and obviously have not been examined here. In future work we hope to examine the consistency of our theory for stationary circulation change with output from comprehensive GCMs having realistic land–ocean boundary conditions and a seasonal cycle of insolation. If found to be relevant to comprehensive GCM simulations, this mechanism could provide a new understanding for the sensitivity of stationary circulation and hydrology to climate change.

*Acknowledgments.* Both authors were supported by National Science Foundation Division of Atmospheric and Geospace Sciences Grants AGS-1253222 and AGS-1515960, and X. Levine acknowledges support from a Yale Climate and Energy Institute (YCEI) postdoctoral fellowship. This work was supported in part by the facilities and staff of the Yale University Faculty of Arts and Sciences High Performance Computing Center. We thank Benjamin R. Lintner for helpful discussion on the first-baroclinic mode theory. Insightful comments from three anonymous reviewers improved the manuscript.

## APPENDIX

### A Derivation of the Temperature Mode

Here we derive an analytical expression for the temperature mode  $A_1$  and discuss its detailed sensitivity to LCL temperature. We assume that  $A_1$  is horizontally uniform, in agreement with the near invariance of the convective lapse rate across the tropics. Following NZ, we also assume that the LCL, which defines the top of

the subcloud layer, is invariant to climate change; its pressure is set to 850 hPa. LCL pressure varies little in our simulations, in agreement with near-surface relative humidity varying by less than 10% in our simulations. We use the assumptions described in section 4b with a definition of saturation moist static energy (MSE)  $h_{\text{sat}}$ :

$$h_{\text{sat}} = T + \frac{g}{c_p} z + \frac{L_v}{c_p} q_{\text{sat}}. \quad (\text{A1})$$

Here  $c_p$  is the specific heat of dry air at constant pressure,  $L_v$  is the latent heat of vaporization of water,  $z$  is the geopotential height, and  $q_{\text{sat}}$  is the saturation specific humidity. Equation (A1) applies to an atmosphere with no liquid water, consistent with the pseudoadiabatic convective scheme of the GCM. Changes in saturation MSE at a given pressure level may be expressed as a function of local temperature changes:

$$\left. \frac{dh_{\text{sat}}}{dT} \right|_p = 1 + z_T + q_T, \quad (\text{A2})$$

where

$$q_T = \left. \frac{L_v}{c_p} \frac{dq_{\text{sat}}}{dT} \right|_p = \frac{L_v^2 q_r}{c_p r_v T_r^2} \left( 1 + \frac{r_v}{r_d} q_r - q_r \right) \quad \text{and}$$

$$z_T = \left. \frac{g}{c_p} \frac{dz}{dT} \right|_p = -\frac{r_d}{c_p} \log \frac{p}{p_s}. \quad (\text{A3})$$

Here  $r_v$  is the specific gas constant for water vapor. Hydrostatic balance was used to express the geopotential height sensitivity  $z_T$  in terms of pressure. The variables  $T_r$  and  $q_r$  are temperature and saturation specific humidity near the heat source (i.e., zonally averaged over 20°–30°N). We then obtain an expression for the sensitivity of tropospheric temperature to changes in saturation MSE:

$$\left. \frac{dT}{dh_{\text{sat}}} \right|_p = \frac{1}{1 + z_T + q_T}. \quad (\text{A4})$$

In convective quasi equilibrium (QE), variations in saturation MSE are invariant with height above the LCL and are equal to variations in subcloud-layer MSE (e.g., Emanuel 2007). Combining (A4) with this QE postulate allows us to express free-tropospheric temperature changes in terms of LCL temperature changes:

$$A_1 = \left. \frac{dT}{dT_b} \right|_p = \left. \frac{dT}{dh_{\text{sat}}} \right|_p \left( \left. \frac{dh_{\text{sat}}}{dT} \right|_p \right)^{-1}$$

$$= \frac{1 + (z_T)_b + (q_T)_b}{1 + z_T + q_T}, \quad (\text{A5})$$

where the subscript  $b$  indicates evaluation at the LCL. Further simplifications of (A5) are possible, as is done by NZ when deriving a temperature mode for their Quasi-Equilibrium Tropical Circulation Model (QTCM). NZ's approximation of the temperature mode gives a near identical profile to that obtained from its more general form (A5) in Earthlike climates, except in the upper troposphere where profiles differ because of the geopotential term  $z_T$  becoming comparable to the moisture term  $q_T$  (NZ's formulation assumes  $z_T \ll q_T$ ). Furthermore, NZ's formulation uses a simplified version of the pseudoadiabatic lapse rate that does not account fully for the effect of moisture in the warmest simulations. Hence, the temperature mode in this study is defined by (A5) instead of that given by NZ.

Equation (A5) shows that the temperature mode is greater than 1 in the troposphere and increases with height at most levels below the tropopause. Its amplitude changes nonmonotonically with tropical mean temperature in a fashion determined by the temperature dependence of saturation specific humidity (Fig. 6, left).

## REFERENCES

- Betts, A. K., 1998: Climate-convection feedbacks: Some further issues. *Climate Change*, **39**, 35–38, doi:10.1023/A:1005323805826.
- Boos, W. R., 2012: Thermodynamic scaling of the hydrological cycle of the Last Glacial Maximum. *J. Climate*, **25**, 992–1006, doi:10.1175/JCLI-D-11-00010.1.
- Chen, T.-C., 2010: Characteristics of summer stationary waves in the Northern Hemisphere. *J. Climate*, **23**, 4489–4507, doi:10.1175/2010JCLI3149.1.
- Cherchi, A., A. Alessandri, S. Masina, and A. Navarra, 2011: Effects of increased CO<sub>2</sub> levels on monsoons. *Climate Dyn.*, **37**, 83–101, doi:10.1007/s00382-010-0801-7.
- Chou, C., and J. D. Neelin, 2004: Mechanisms of global warming impacts on regional tropical precipitation. *J. Climate*, **17**, 2688–2701, doi:10.1175/1520-0442(2004)017<2688:MOGWIO>2.0.CO;2.
- , and C. A. Chen, 2010: Depth of convection and the weakening of tropical circulation in global warming. *J. Climate*, **23**, 3019–3030, doi:10.1175/2010JCLI3383.1.
- Collins, M., and Coauthors, 2013: Long-term climate change: Projections, commitments and irreversibility. *Climate Change 2013: The Physical Science Basis*, T. F. Stocker et al., Eds., Cambridge University Press, 1029–1136.
- Douville, H., F. Chauvin, S. Planton, J. F. Royer, D. Salas-Melia, and S. Tyteca, 2002: Sensitivity of the hydrological cycle to increasing amounts of greenhouse gases and aerosols. *Climate Dyn.*, **20**, 45–68, doi:10.1007/s00382-002-0259-3.
- Durack, P. J., S. E. Wijffels, and R. J. Matear, 2012: Ocean salinities reveal strong global water cycle intensification during 1950 to 2000. *Science*, **336**, 455–458, doi:10.1126/science.1212222.
- Emanuel, K. A., 2007: Quasi-equilibrium dynamics of the tropical atmosphere. *The Global Circulation of the Atmosphere*, T. Schneider and A. H. Sobel, Eds., Princeton University Press, 186–218.

- Frierson, D. M. W., 2007: The dynamics of idealized convection schemes and their effect on the zonally averaged tropical circulation. *J. Atmos. Sci.*, **64**, 1959–1976, doi:[10.1175/JAS3935.1](https://doi.org/10.1175/JAS3935.1).
- , I. M. Held, and P. Zurita-Gotor, 2006: A gray-radiation aquaplanet moist GCM. Part I: Static stability and eddy scale. *J. Atmos. Sci.*, **63**, 2548–2566, doi:[10.1175/JAS3753.1](https://doi.org/10.1175/JAS3753.1).
- Gill, A. E., 1980: Some simple solutions for heat-induced tropical circulation. *Quart. J. Roy. Meteor. Soc.*, **106**, 447–462, doi:[10.1002/qj.49710644905](https://doi.org/10.1002/qj.49710644905).
- Held, I. M., and B. J. Soden, 2006: Robust responses of the hydrological cycle to global warming. *J. Climate*, **19**, 5686–5699, doi:[10.1175/JCLI3990.1](https://doi.org/10.1175/JCLI3990.1).
- Horinouchi, T., 2012: Moist Hadley circulation: Possible role of wave–convection coupling in aquaplanet experiments. *J. Atmos. Sci.*, **69**, 891–907, doi:[10.1175/JAS-D-11-0149.1](https://doi.org/10.1175/JAS-D-11-0149.1).
- Hoskins, B. J., and D. J. Karoly, 1981: The steady linear response of a spherical atmosphere to thermal and orographic forcing. *J. Atmos. Sci.*, **38**, 1179–1196, doi:[10.1175/1520-0469\(1981\)038<1179:TSLROA>2.0.CO;2](https://doi.org/10.1175/1520-0469(1981)038<1179:TSLROA>2.0.CO;2).
- Joseph, R., M. Ting, and P. J. Kushner, 2004: The global stationary wave response to climate change in a coupled GCM. *J. Climate*, **17**, 540–556, doi:[10.1175/1520-0442\(2004\)017<0540:TGSWRT>2.0.CO;2](https://doi.org/10.1175/1520-0442(2004)017<0540:TGSWRT>2.0.CO;2).
- Kirtman, B. P., and E. K. Schneider, 2000: A spontaneously generated tropical atmospheric general circulation. *J. Atmos. Sci.*, **57**, 2080–2093, doi:[10.1175/1520-0469\(2000\)057<2080:ASGTAG>2.0.CO;2](https://doi.org/10.1175/1520-0469(2000)057<2080:ASGTAG>2.0.CO;2).
- Knutson, T. R., and S. Manabe, 1995: Time-mean response over the tropical Pacific to increased CO<sub>2</sub> in a coupled ocean–atmosphere model. *J. Climate*, **8**, 2181–2199, doi:[10.1175/1520-0442\(1995\)008<2181:TMROTT>2.0.CO;2](https://doi.org/10.1175/1520-0442(1995)008<2181:TMROTT>2.0.CO;2).
- Levine, X. J., and T. Schneider, 2011: Response of the Hadley circulation to climate change in an aquaplanet GCM coupled to a simple representation of ocean heat transport. *J. Atmos. Sci.*, **68**, 769–783, doi:[10.1175/2010JAS3553.1](https://doi.org/10.1175/2010JAS3553.1).
- Li, W., L. Li, M. Ting, and Y. Liu, 2012: Intensification of Northern Hemisphere subtropical highs in a warming climate. *Nat. Geosci.*, **5**, 830–834, doi:[10.1038/ngeo1590](https://doi.org/10.1038/ngeo1590).
- Ma, J., S. P. Xie, and Y. Kosaka, 2012: Mechanisms for tropical tropospheric circulation change in response to global warming. *J. Climate*, **25**, 2979–2994, doi:[10.1175/JCLI-D-11-00048.1](https://doi.org/10.1175/JCLI-D-11-00048.1).
- Merlis, T. M., and T. Schneider, 2011: Changes in zonal surface temperature gradients and Walker circulations in a wide range of climates. *J. Climate*, **24**, 4757–4768, doi:[10.1175/2011JCLI4042.1](https://doi.org/10.1175/2011JCLI4042.1).
- Mitchell, J. F. B., C. A. Wilson, and W. M. Cunningham, 1987: On CO<sub>2</sub> climate sensitivity and model dependence of results. *Quart. J. Roy. Meteor. Soc.*, **113**, 293–322, doi:[10.1002/qj.49711347517](https://doi.org/10.1002/qj.49711347517).
- Neelin, J. D., 2007: Moist dynamics of tropical convection zones in monsoons, teleconnections, and global warming. *The Global Circulation of the Atmosphere*, T. Schneider and A. H. Sobel, Eds., Princeton University Press, 267–301.
- , and N. Zeng, 2000: A quasi-equilibrium tropical circulation model—formulation. *J. Atmos. Sci.*, **57**, 1741–1766, doi:[10.1175/1520-0469\(2000\)057<1741:AQETCM>2.0.CO;2](https://doi.org/10.1175/1520-0469(2000)057<1741:AQETCM>2.0.CO;2).
- O’Gorman, P. A., and T. Schneider, 2008: The hydrological cycle over a wide range of climates simulated with an idealized GCM. *J. Climate*, **21**, 3815–3832, doi:[10.1175/2007JCLI2065.1](https://doi.org/10.1175/2007JCLI2065.1).
- , R. P. Allan, M. P. Byrne, and M. Previdi, 2012: Energetic constraints on precipitation under climate change. *Surv. Geophys.*, **33**, 585–608, doi:[10.1007/s10712-011-9159-6](https://doi.org/10.1007/s10712-011-9159-6).
- Peixoto, J. P., and A. H. Oort, 1992: Observed mean state of the atmosphere. *Physics of Climate*, J. P. Peixoto and A. H. Oort, Eds., Springer-Verlag, 131–175.
- Pierrehumbert, R. T., H. Brogniez, and R. Roca, 2007: On the relative humidity of the atmosphere. *The Global Circulation of the Atmosphere*, T. Schneider and A. H. Sobel, Eds., Princeton University Press, 143–185.
- Plumb, R. A., and A. Y. Hou, 1992: The response of a zonally symmetric atmosphere to subtropical thermal forcing: Threshold behavior. *J. Atmos. Sci.*, **49**, 1790–1799, doi:[10.1175/1520-0469\(1992\)049<1790:TROAZS>2.0.CO;2](https://doi.org/10.1175/1520-0469(1992)049<1790:TROAZS>2.0.CO;2).
- Rodwell, M. J., and B. J. Hoskins, 1996: Monsoons and the dynamics of deserts. *Quart. J. Roy. Meteor. Soc.*, **122**, 1385–1404, doi:[10.1002/qj.49712253408](https://doi.org/10.1002/qj.49712253408).
- , and —, 2001: Subtropical anticyclones and summer monsoons. *J. Climate*, **14**, 3192–3211, doi:[10.1175/1520-0442\(2001\)014<3192:SAASM>2.0.CO;2](https://doi.org/10.1175/1520-0442(2001)014<3192:SAASM>2.0.CO;2).
- Scheff, J., and D. M. W. Frierson, 2012: Robust future precipitation declines in CMIP5 largely reflect the poleward expansion of model subtropical dry zones. *Geophys. Res. Lett.*, **39**, L18704, doi:[10.1029/2012GL052910](https://doi.org/10.1029/2012GL052910).
- Schneider, T., P. A. O’Gorman, and X. J. Levine, 2010: Water vapor and the dynamics of climate changes. *Rev. Geophys.*, **48**, RG3001, doi:[10.1029/2009RG000302](https://doi.org/10.1029/2009RG000302).
- Seager, R., N. Naik, and G. A. Vecchi, 2010: Thermodynamic and dynamic mechanisms for large-scale changes in the hydrological cycle in response to global warming. *J. Climate*, **23**, 4651–4668, doi:[10.1175/2010JCLI3655.1](https://doi.org/10.1175/2010JCLI3655.1).
- Shaw, T. A., 2014: On the role of planetary-scale waves in the abrupt seasonal transition of the Northern Hemisphere general circulation. *J. Atmos. Sci.*, **71**, 1724–1746, doi:[10.1175/JAS-D-13-0137.1](https://doi.org/10.1175/JAS-D-13-0137.1).
- , and O. Pauluis, 2012: Tropical and subtropical meridional latent heat transports by disturbances to the zonal mean and their role in the general circulation. *J. Atmos. Sci.*, **69**, 1872–1889, doi:[10.1175/JAS-D-11-0236.1](https://doi.org/10.1175/JAS-D-11-0236.1).
- Singh, M. S., and P. A. O’Gorman, 2012: Upward shift of the atmospheric general circulation under global warming: Theory and simulations. *J. Climate*, **25**, 8259–8276, doi:[10.1175/JCLI-D-11-00699.1](https://doi.org/10.1175/JCLI-D-11-00699.1).
- Sobel, A. H., J. Nilsson, and L. M. Polvani, 2001: The weak temperature gradient approximation and balanced tropical moisture waves. *J. Atmos. Sci.*, **58**, 3650–3665, doi:[10.1175/1520-0469\(2001\)058<3650:TWTGAA>2.0.CO;2](https://doi.org/10.1175/1520-0469(2001)058<3650:TWTGAA>2.0.CO;2).
- Tanaka, H. L., N. Ishizaki, and A. Kitoh, 2004: Trend and interannual variability of walker, monsoon and Hadley circulations defined by velocity potential in the upper troposphere. *Tellus*, **56A**, 250–269, doi:[10.1111/j.1600-0870.2004.00049.x](https://doi.org/10.1111/j.1600-0870.2004.00049.x).
- Trenberth, K. E., and D. P. Stepaniak, 2004: The flow of energy through the earth’s climate system. *Quart. J. Roy. Meteor. Soc.*, **130**, 2677–2701, doi:[10.1256/qj.04.83](https://doi.org/10.1256/qj.04.83).
- , —, and J. M. Caron, 2000: The global monsoon as seen through the divergent atmospheric circulation. *J. Climate*, **13**, 3969–3993, doi:[10.1175/1520-0442\(2000\)013<3969:TGMASST>2.0.CO;2](https://doi.org/10.1175/1520-0442(2000)013<3969:TGMASST>2.0.CO;2).
- Troen, I. B., and L. Mahrt, 1986: A simple model of the atmospheric boundary layer; sensitivity to surface evaporation. *Bound.-Layer Meteor.*, **37**, 129–148, doi:[10.1007/BF00122760](https://doi.org/10.1007/BF00122760).
- Ueda, H., A. Iwai, K. Kuwako, and M. E. Hori, 2006: Impact of anthropogenic forcing on the Asian summer monsoon as simulated by eight GCMs. *Geophys. Res. Lett.*, **33**, L06703, doi:[10.1029/2005GL025336](https://doi.org/10.1029/2005GL025336).

- Vecchi, G. A., and B. J. Soden, 2007: Global warming and the weakening of the tropical circulation. *J. Climate*, **20**, 4316–4340, doi:[10.1175/JCLI4258.1](https://doi.org/10.1175/JCLI4258.1).
- Wang, B., and Q. Ding, 2006: Changes in global monsoon precipitation over the past 56 years. *Geophys. Res. Lett.*, **33**, L06711, doi:[10.1029/2005GL025347](https://doi.org/10.1029/2005GL025347).
- Webster, P. J., 1972: Response of the tropical atmosphere to local, steady forcing. *Mon. Wea. Rev.*, **100**, 518–541, doi:[10.1175/1520-0493\(1972\)100<0518:ROTTAT>2.3.CO;2](https://doi.org/10.1175/1520-0493(1972)100<0518:ROTTAT>2.3.CO;2).
- Wentz, F. J., L. Ricciardulli, K. Hilburn, and C. Mears, 2007: How much more rain will global warming bring? *Science*, **317**, 233–235, doi:[10.1126/science.1140746](https://doi.org/10.1126/science.1140746).
- Wills, R. C., and T. Schneider, 2015: Stationary eddies and the zonal asymmetry of net precipitation and ocean freshwater forcing. *J. Climate*, **28**, 5115–5133, doi:[10.1175/JCLI-D-14-00573.1](https://doi.org/10.1175/JCLI-D-14-00573.1).
- Zhai, J., and W. Boos, 2015: Regime transitions of cross-equatorial Hadley circulations with zonally asymmetric thermal forcings. *J. Atmos. Sci.*, **72**, 3800–3818, doi:[10.1175/JAS-D-15-0025.1](https://doi.org/10.1175/JAS-D-15-0025.1).
- Zhou, T., L. Zhang, and H. Li, 2008: Changes in global land monsoon area and total rainfall accumulation over the last half century. *Geophys. Res. Lett.*, **35**, L16707, doi:[10.1029/2008GL034881](https://doi.org/10.1029/2008GL034881).
- Zhou, Y. P., K. M. Xu, Y. C. Sud, and A. K. Betts, 2011: Recent trends of the tropical hydrological cycle inferred from Global Precipitation Climatology Project and International Satellite Cloud Climatology Project data. *J. Geophys. Res.*, **116**, D09101, doi:[10.1029/2010JD015197](https://doi.org/10.1029/2010JD015197).